Journal of Fluids and Structures 82 (2018) 154–172

Contents lists available at ScienceDirect

Journal of Fluids and Structures

journal homepage: www.elsevier.com/locate/jfs

Multi-mode responses, rivulet dynamics, flow structures and mechanism of rain-wind induced vibrations of a flexible cable

Donglai Gao [a,b,c], Wenli Chen [a,b,*], Christophe Eloy [c], Hui Li [a,b]

[a] Key Lab of Smart Prevention and Mitigation of Civil Engineering Disasters of Ministry of Industry and Information Technology, Harbin Institute of Technology, Harbin, 150090, China

[b] Key Lab of Structures Dynamic Behavior and Control of Ministry of Education, Harbin Institute of Technology, Harbin, 150090, China

[c] Aix-Marseille Univ, CNRS, Centrale Marseille, IRPHE, Marseille, 13013, France

A R T I C L E I N F O

Article history:
Received 19 November 2017
Received in revised form 29 May 2018
Accepted 29 June 2018

Keywords:
Rain-wind induced vibrations
Multi-mode responses
Upper rivulet dynamics
Flow structures
Bubble burst

A B S T R A C T

We successfully excite the multi-mode rain-wind induced vibrations (RWIVs) of a flexible stay cable in a wind tunnel by guiding water rivulets along the cable surface. The first, second and third mode RWIVs are excited respectively by increasing the incoming wind speed. The movement of upper rivulet during the first, second and third mode RWIVs are recorded with a high-speed camera. By employing a computer vision based recognition technique, the upper-rivulet dynamics of different modes of RWIVs are recognized and analyzed. The wake flow structures around the dry cable and the cable suffering from RWIVs are measured by using a particle image velocimetry (PIV) system. Experiment results show that the oscillation frequency of the upper rivulet is synchronized with the cable vibration frequency for the first, second and third mode RWIVs. Based on experiment results, bubble burst is proposed as a possible mechanism for the excitation of RWIVs.

1. Introduction

Thirty years ago, Hikami and Shiraishi (1988) observed that the stay cables of Meikonishi Bridge experienced large amplitude vibrations under the joint action of rain and wind. The observed cable vibrations are neither conventional von Kármán vortex induced vibration (VIV) nor wake galloping (WG) since the vibration frequency is much lower than the Strouhal frequency shed from the cable and the gap between cables is too large to excite wake galloping. This new type of cable vibration under the joint action of rain and wind has been called rain-wind induced vibration (RWIV). Rainfall was shown through wind tunnel tests to induce the formation of a rivulet along the cable surface, which plays an crucial role in the aerodynamic instability of the stay cable. After the findings of Hikami and Shiraishi (1988), the same RWIV phenomenon has been reported in a number of cable-stayed bridges around the world, such as Tenpozan Bridge (Japan, Matsumoto, 1989), Erasmus Bridge (Hollande, Geurts et al., 1998), Faro Bridge in Denmark, Dongting Lake Bridge (P. R. China, Ni et al., 2007), and Fred Hartman Bridge (United States, Zuo et al., 2008). RWIVs have attracted extensive research interests, for their great vibration amplitudes may affect the durability and service life of cable-stayed bridges. However, the excitation mechanism of RWIVs is still a matter of debate.

According to previous studies (Matsumoto et al., 2005; Gu, 2009), the dynamics of the upper rivulet formed on the cable surface plays a crucial role in the excitation of RWIVs. Therefore, several wind tunnel tests have been conducted to investigate the morphology and dynamics of water rivulets (Cosentino et al., 2003a, b; Li et al., 2010a, 2015; Jing et al., 2015, 2017, 2018). However, experimental measurements on upper rivulet in the wind tunnel tests are not easy to carry out. Therefore, some

* Corresponding author.
E-mail address: cwl_80@hit.edu.cn (W. Chen).

https://doi.org/10.1016/j.jfluidstructs.2018.06.017
0889-9746/

theoretical models have been proposed to address the effects of an upper rivulet analytically. Yamaguchi (1990) proposed a numerical model to simulate RWIVs, from the perspective of galloping instability. Based on the experimentally measured aerodynamics and structural dynamics of RWIV, Xu and Wang (2003) developed a model to consider the effect of mean wind speed on the position of upper rivulet and the influence of moving upper rivulet on cable vibration. They proposed that due to the negative aerodynamic damping, the vibration amplitude of the circular cylinder with a fixed artificial rivulet is amplified. Xu et al. (2006) investigated the aerodynamic coefficients of the cable model with different locations of artificial rivulet. It was observed that the negative slope in the lift coefficient curve might be responsible for the occurrence of potential RWIV. Gu and Huang (2008) considered the RWIV phenomenon by attaching an artificial rivulet onto the smooth cylinder surface to simulate the water rivulet. They applied Lyapunov stability theory to derive the criterion for predicting the balance angle of the attachment. Gu (2009) conducted a wind tunnel test to measure the wind pressures acting on a cable and its upper artificial rivulet. Then he established a numerical model with a moving upper rivulet based on the quasi-steady assumption. The model predicted substantial variations of the wind forces acting on the cable model at some particular rivulet positions, which might be the key to the understanding of RWIVs. Du et al. (2013) attached an artificial upper rivulet to an inclined and yawed circular cylinder to measure the wind pressure distributions and wind forces acting both on the artificial rivulet and the cable. Similarly to Gu (2009), they observed dramatic variations of the aerodynamic forces acting on the cable as the upper rivulet was shifted to different positions.

It should be noted that the artificial rivulets are preselected with different shapes (for instance, semi-elliptic by Xu et al. (2006), hollow tube by Gu and Huang (2008), and arch-shaped by Gu (2009) and the size of artificial rivulet is mostly larger than its actual scales (Gu, 2009) in the previous studies. Therefore, the morphology evolution of water film on the cable surface cannot be simulated properly by artificial rivulets. Besides, the artificial rivulet is assumed fixed in most simulations and experiments of the cable-rivulet system, as reviewed above. Yet, the morphology evolution and dynamics of rivulet are also important. Some other previous studies thus focused on the formation and evolution of water film on the surface of a circular cylinder and their influences on aerodynamic forces. Lemaitre et al. (2007) first formulated the governing equations for the water film on the cylinder surface. The theoretical model developed by Lemaitre et al. (2007) could predict the locations of rivulets at given conditions (Lemaitre et al., 2010), but not the circumferential movement of rivulets around the cylinder. The reason is that they adopted constant pressure ($C_p(\theta)$) and friction ($C_f(\theta)$) coefficients measured by Achenbach (1968) to solve the governing system. Though the theoretically predicted positions were found in excellent agreement with experiment results, the periodic oscillation of rivulets could not be predicted. Because these two aerodynamic coefficients are time-varying and they have a great influence on the evolution of the upper water film, Robertson et al. (2010) and Taylor and Robertson (2011) extended Lemaitre's model and numerically solved the instantaneous and time-dependent wind pressure ($C_p(\theta, t)$) and friction ($C_f(\theta, t)$) coefficients to substitute them into the governing system. As such, the detailed simulations of the RWIV phenomenon were realized by solving this coupled system. According to these articles, a small rivulet is formed on the upper surface and evolves periodically. More recently, Bi et al. (2013, 2014) and Wang et al. (2016) combined Lemaitre's model and Computational Fluid Dynamics (CFD) techniques to conduct serial studies and reveal some important features of RWIV. They confirmed that only within a particular wind speed range, the upper rivulet formed on the surface of the cable could evolve periodically, resulting in a periodically changing aerodynamic lift force acting on the cable model, which could lead to large amplitude vibrations. On the other hand, the oscillation frequency of upper rivulet was distinctly different from the cable's natural frequency outside of this wind speed range, yielding small-amplitude cable vibration in this case. They concluded that the RWIV only occurred in a particular range of wind speed with the oscillation frequency of water film being close to the cable frequency, which was consistent with field monitoring observations.

Although the excitation mechanism of the RWIV has yet to be clarified, it is clear that the vibration energy is obtained from the fluid–structure system. To gain more insight into the transfer of energy from the fluid to the cable, the interaction between the cable and the flow (both air and water) has been studied. Wang et al. (2005) investigated the formation of water rivulets running along a circular cylinder subject to wind and its effects on the near-wake flow to find that the formation of water rivulets on the cylinder surface increases notably the normalized dominant frequencies in the near wake. They proposed that the large circumferential oscillation of the water rivulets might act as a periodic perturbation influencing the flow separation from the cylinder.

When a strong adverse pressure gradient occurs on a cylinder surface, the laminar boundary layer is to separate from the curved surface to form a separation bubble. Separation bubbles on an airfoil can be divided into two types: a short bubble characterized by reattachment of separated flow, and a long bubble characterized by detachment of the separated flow. When the short bubble fails to reattach onto the airfoil surface, a *bubble burst* takes place. As a result of the bubble burst and flow detachment, a sudden decrease of the lift will occur. This phenomenon is often referred to as *stall* in aeronautical engineering. In the experiments of Zaman et al. (1989), they found that when the stall of flow over an airfoil was deeply developed, i.e., at the angle of attack AOA$\geq$18°, the vortex shedding form the airfoil was characterized with a Strouhal number, $St \approx 0.2$. However, at the onset AOA of static stall, approximately AOA=15°, a periodic oscillation characterized by much lower (one order of magnitude) frequency was observed. Apparently, this phenomenon of transition (great decrease) must be associated with a transitional state of the bubble burst (stall). Based on previous studies (Zaman et al., 1989; Alam and Sandham, 2000; Rinoie and Takemura, 2004), the general aspects of the stall phenomenon of airfoils can be summarized as: (1) a sudden and dramatic reduction in the lift force due to the flow detachment; (2) a much lower frequency of vortex shedding and lift force; (3) bubble burst, i.e., transition from short bubble (reattachment-type) to long bubble (detachment-type); (4) mitigation and even complete modification to the von Kármán vortex shedding; (5) the stall is closely related

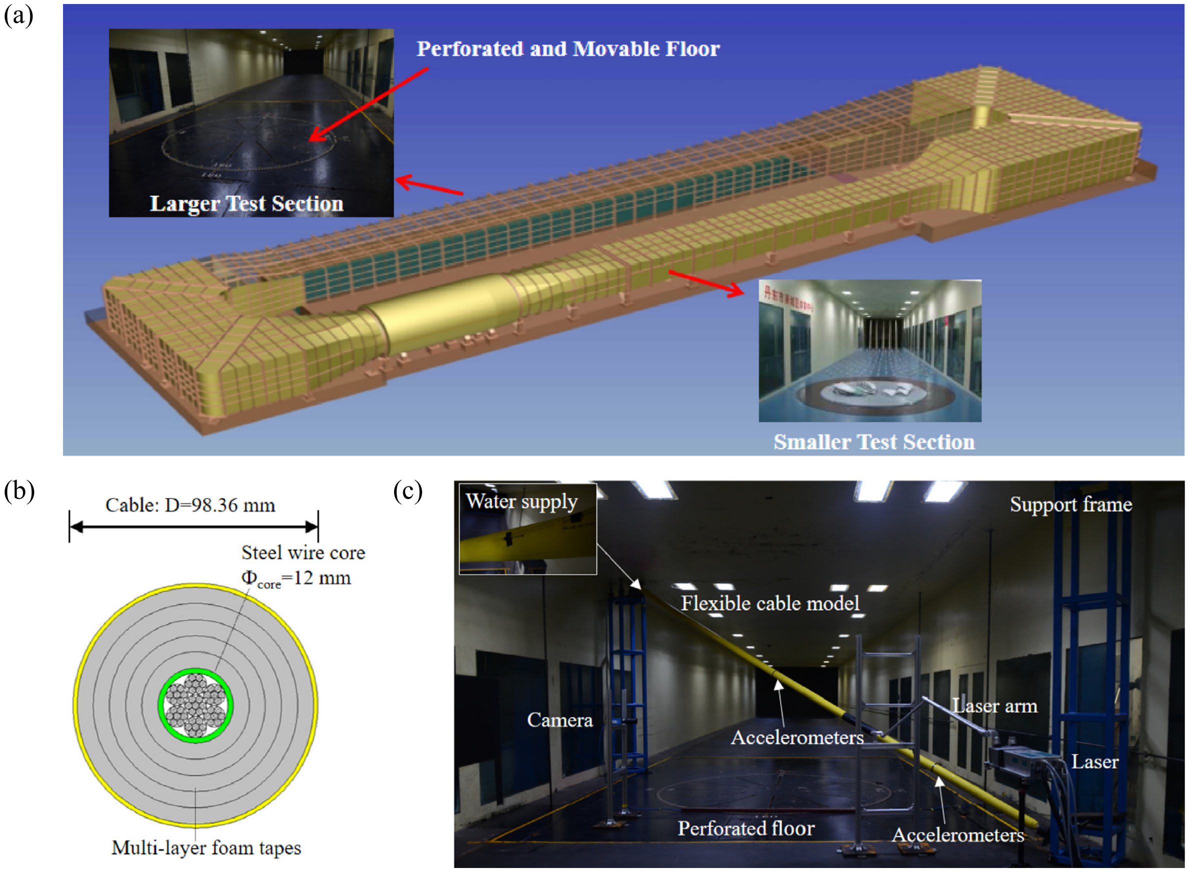

Fig. 1. Cable model and experimental setup: (a) sketch of the WTWF laboratory; (b) cross-section of the flexible cable model, the diameters of the cable and the steel wire core are unscaled; and (c) the cable model tensioned in the larger test section.

to shear layer instability (for instance, Kelvin–Helmholtz instability), though its working mechanism has not been clearly addressed. The first aspect explains why stall is a vital concern to aeronautical engineering and has attracted intensive research interests, while the latter characteristics are related to its generation mechanism.

In the present study, we reproduced the multi-mode rain-wind induced vibrations of a flexible cable in a wind tunnel. The context below is organized as follows: a brief introduction to the experimental setup is given in Section 2, experiment results, including multi-mode cable behaviors, upper-rivulet dynamics and flow structures are presented and analyzed in Section 3, bubble burst is proposed as a possible excitation mechanism of RWIVs in Section 4, and some concluding remarks are drawn in Section 5.

2. Experimental setup

The experiment study was conducted in the larger test section of Joint Laboratory of Wind Tunnel and Wave Flume (WTWF), Harbin Institute of Technology, P. R. China. The closed-loop wind tunnel has two test sections, a smaller one and a larger one, as shown in Fig. 1(a). The dimension of the larger one is 6.0 m (width) × 3.6 m (height) with a length of 50 m. The wave flume, which is as deep as 4.5 m, has been constructed beneath the movable and perforated floor of the larger test section, as can be noticed in Fig. 1(c)). The perforated floor facilitates an immediate water drainage into the wave flume and therefore the experimental study of RWIVs. The incoming turbulence intensity of the airflow in the larger test section is about 0.7%.

2.1. Flexible cable model

A cable with a length L of 8.31 m and a diameter D of 98.36 mm is manufactured to reproduce RWIVs. This cable model is made with a 12-mm diameter steel wire core and multiple layers of foam taps wrapped around it, as shown in Fig. 1(b). A heat-shrink Polyethylene (PE) tube, with an arithmetical mean deviation of the profile Ra = 1.6 μm, is used as the outside coating to create a smooth surface of the cable. The roundness error of the cable model is measured to be about 1.0 mm. In

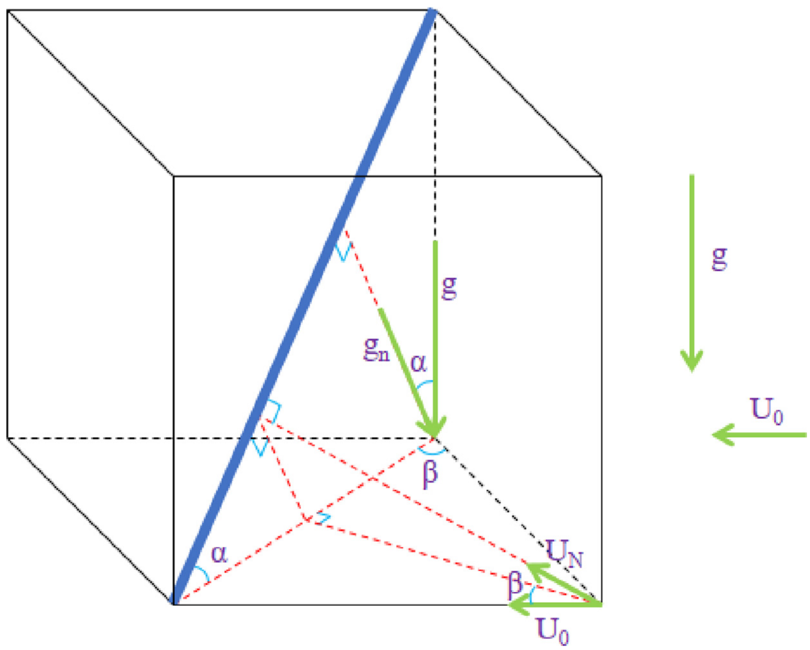

Fig. 2. Spatial position of the stay cable in the wind tunnel, α is the inclination angle and β is the yaw angle.

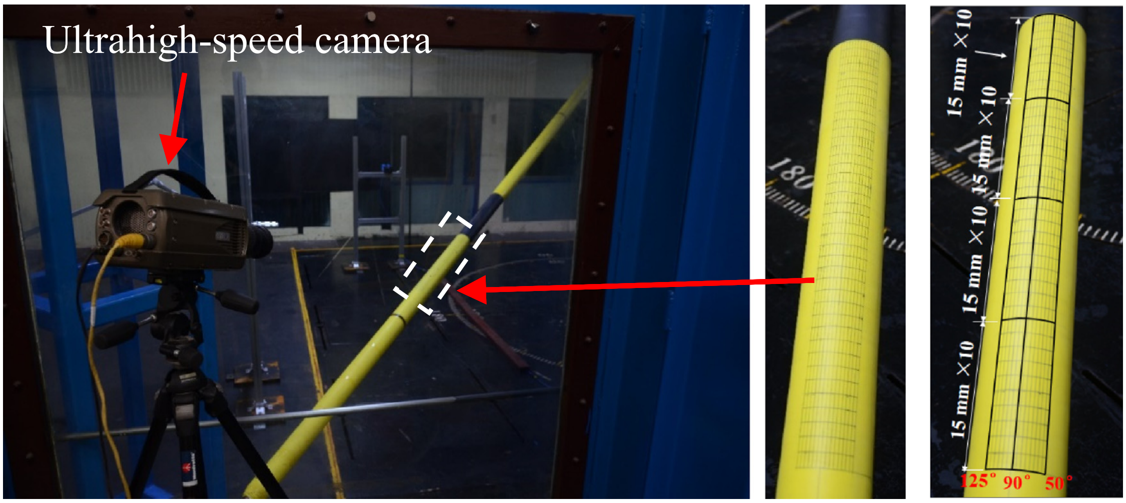

Fig. 3. Experimental setup for upper-rivulet monitoring.

the wind tunnel tests, the yaw angle (defined in Fig. 2) is set to be 45° as in Hikami and Shiraishi (1988) and its inclination angle (also defined in Fig. 2) is then determined to be 23.39°. The long and flexible cable model is tensioned through the steel wire core and fixed to the upper and lower end plates supported by two separated steel frames. The rigid support frames are placed on the tunnel floor and firmly fixed to the tunnel ceiling by eight specially designed brakes to avoid any movement or displacement of the support frames. Four accelerometers (B&K 4507B) are used to measure the in-plane and out-of-plane vibration responses of the flexible cable. Two accelerometers are fixed at the position of $L/2$, while the other two accelerometers are fixed near $L/6$ in the same manner. They are all neatly wrapped by water-resistant tapes to maintain their working performance with the water rivulet running on the cable, as shown in Fig. 1(c). The sampling rate for vibration tests is 1000 Hz. Free vibration tests are first conducted in the still air to obtain structural parameters of the flexible cable model. Based on free vibration signals, the natural frequencies and damping ratios are identified and the results are given in Table 1. In addition, the mass of the cable model is measured to be 1.03 kg/m. The Scruton number is calculated to be: $S_c = m\xi/\rho D^2 = 0.33$ (where m is the mass; ξ the damping ratio, ρ the air density and D the cable diameter). It can be seen

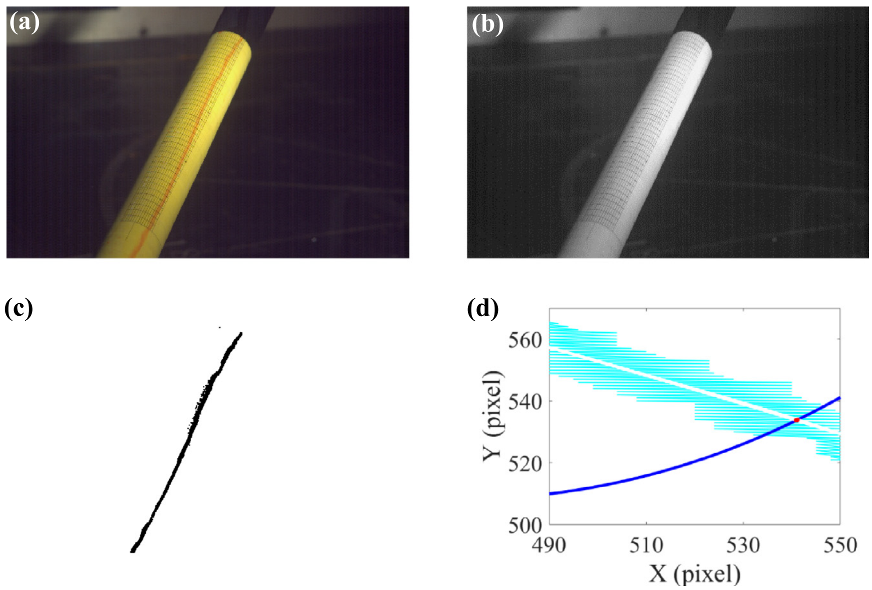

Fig. 4. Identification of upper rivulet by background subtraction (Fig.(a) subtracts Fig.(b) → Fig.(c)) and identification of the position of upper rivulet (Fig.(d)).

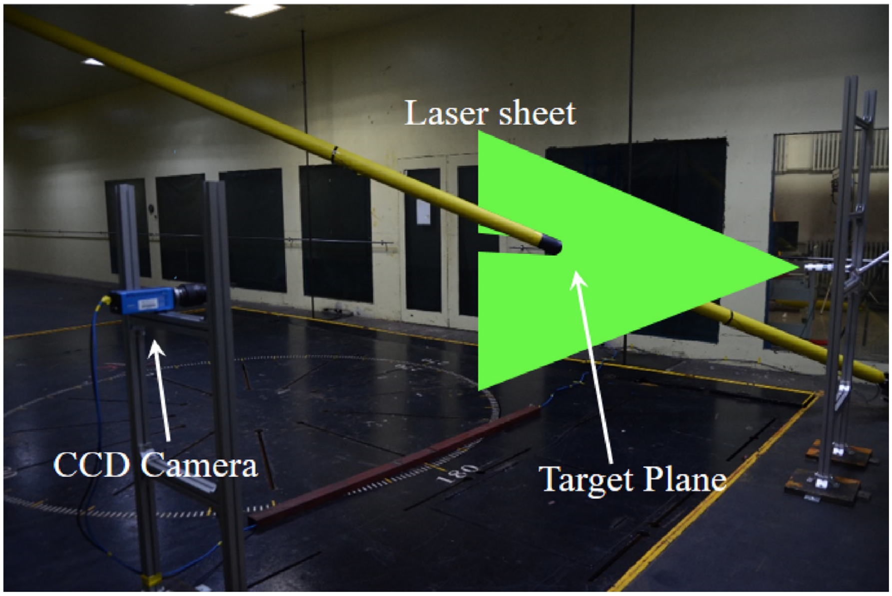

Fig. 5. Experimental setup for PIV measurement.

that low mass and low damping ratio (and therefore low S_c) of the cable contribute to the excitation of RWIVs in the wind tunnel tests.

2.2. Upper rivulet monitoring

It has been verified by Jing et al. (2015) that guiding water lines has the same function as spraying water in the wind tunnel tests of RWIVs. Applying this approach to form an upper rivulet and thus excite RWIVs has an obvious advantage when conducting PIV measurements, since there is no real rainfall during the tests. In the present study, a flexible plastic tube with an inner diameter of 5 mm is used to form water rivulets, as shown in Fig. 1(c). It is glued onto the upper end of the stay cable. The water is colored with red ink for observation and identification. A large tank filled with colored water is

Table 1
Modal frequencies and damping ratios of the flexible cable model.

Mode	In-plane		Out-of-Plane	
	Frequency (Hz)	Damping ratio (%)	Frequency (Hz)	Damping ratio (%)
First	2.347	0.3979	2.136	0.3885
Second	4.425	0.4013	4.272	0.3903
Third	6.622	/	6.607	/

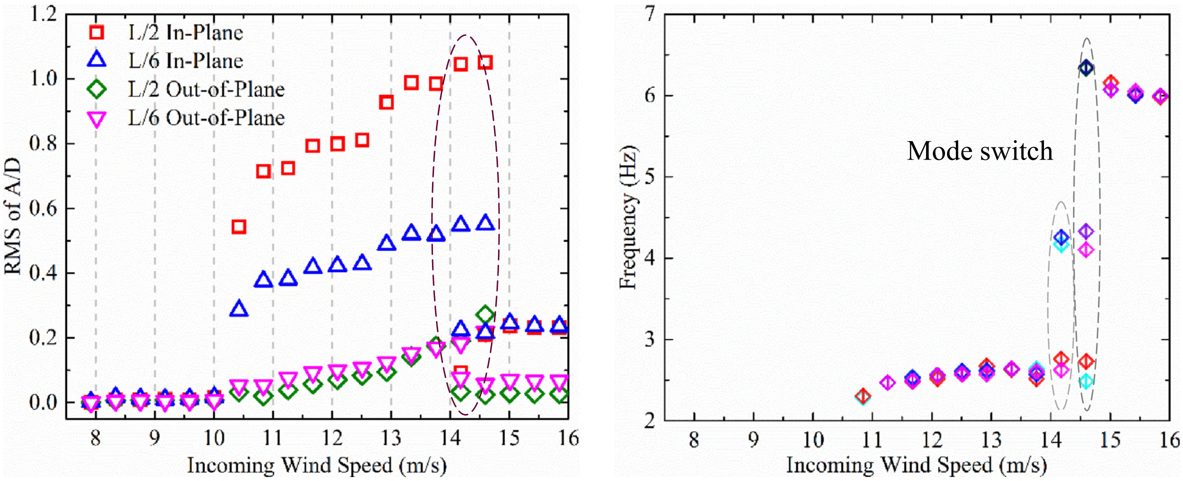

Fig. 6. Vibration amplitudes (left) and dominant frequencies (right) of the flexible cable model with the increase of wind speed.

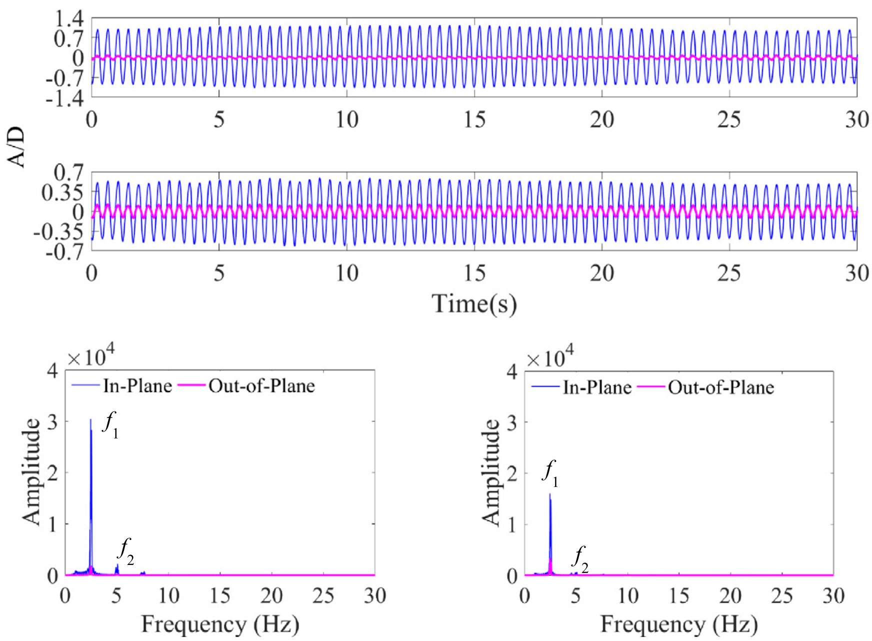

Fig. 7. The first mode displacement responses (up) and frequency spectrum (down) at $U = 11.26$ m·s^{-1}, up-top: $L/2$; up-bottom: $L/6$; down-left: $L/2$; down-right: $L/6$. $f_1 = 2.47$ Hz, $f_2 = 5.08$ Hz. The blue lines denote the in-plane vibrations and the magenta lines denote the out-of-plane vibrations. (For interpretation of the references to color in this figure legend, the reader is referred to the web version of this article.)

placed on top of the wind tunnel and the water flow could be controlled by a valve. In the present study, the flow rate (Q) from the water tube is constant and measured to be 21.14 ml/s. During RWIVs, the lower rivulet is found to be thick and resulted in an additional mass to the cable. Since it is expected to have little effects on RWIVs and it is difficult to measure

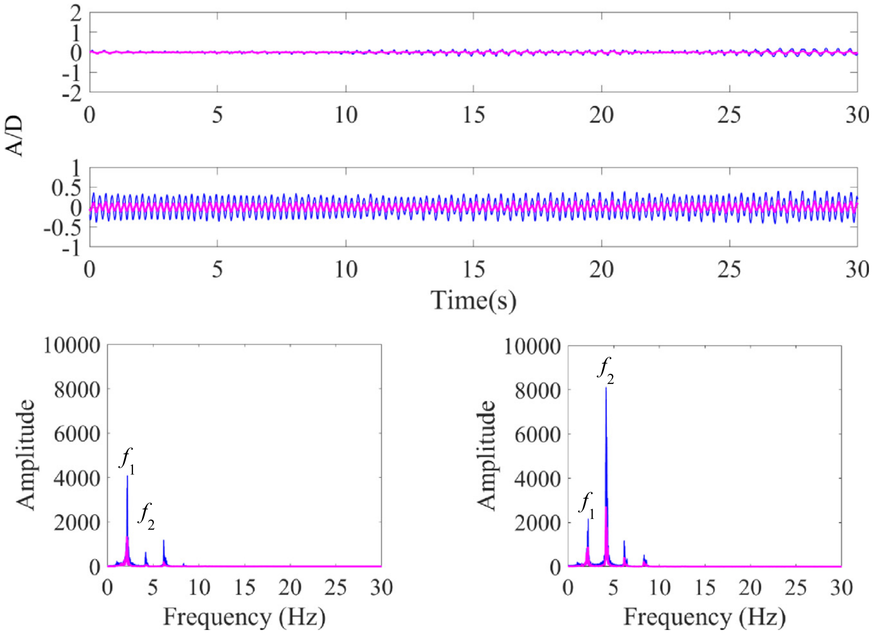

Fig. 8. The second mode displacement responses (up) and frequency spectrum (down) at $U = 14.18$ m·s^{-1}, up-top: $L/2$; up-bottom: $L/6$; down-left: $L/2$; down-right: $L/6$. $f_1 = 2.19$ Hz, $f_2 = 4.17$ Hz, $f_3 = 6.16$ Hz. The blue lines denote the in-plane vibrations and the magenta lines denote the out-of-plane vibrations. (For interpretation of the references to color in this figure legend, the reader is referred to the web version of this article.)

and study the lower rivulet qualitatively, we neglect the effects of lower rivulet and focus on the upper rivulet in the present paper.

To monitor and investigate the formation and oscillation of the upper rivulet, a measurement region is defined slightly above the $L/6$ knot on the cable surface, as shown in Fig. 3. This location allowed the upper rivulet to be fully developed along the cable. A grid system is plotted onto the cable surface and it is moving with the cable. The circumferential grid increases form 50° to 125° (0° is defined as the windward standpoint) with an increment of 5° while the longitudinal length unit is 15 mm. During the wind tunnel tests, a high-speed camera (Phantom V310) is employed to monitor and record the images of the measurement region. The high-speed camera is fixed outside the test section and the image acquisition is performed through the transparent wall, as shown in Fig. 3. The image resolution is 800 × 1200 pixels, and its sampling frequency is set at 200 frames per second, which is much higher than the oscillation frequency of upper rivulet.

At each instant, the upper rivulet can be described by the grid system attached onto the cable. By collecting the instantaneous position of the upper rivulet in the time-domain, the upper rivulet dynamics could be obtained. For each extracted image, the position of the upper rivulet is first identified by a background subtraction (BS) method. The raw images are converted into a series of RGB images. At time t_i, the raw image (Fig. 4(a)) is represented by $I(x, y, t_i)$ and the background (Fig. 4(b)) by $B(x, y, t_i)$, where x and y are Cartesian coordinates of the image plane. The BS method can be described by the following formula:

$$\Gamma(x, y) = \begin{cases} 0, & \text{if} \quad I(x, y, t_i) - B(x, y, t_i) > \tau \\ 1, & \text{otherwise} \end{cases}$$

where τ is a user-defined threshold. By detecting the nonzero elements of $\Gamma(x, y)$, the area of upper rivulet (Fig. 4(c)) can be described as $G(x, y, t_i)$. On the cable surface, the grid system is denoted by $\Omega(x, y, \theta, t_i)$, where x and y are Cartesian coordinates of the image plane, while r and θ are adopted to characterize the position of upper rivulet. The position of rivulet (r, θ) can be obtained by the one-to-one mapping: $G(x, y, t_i) \leftrightarrow \Omega(x, y, \theta, t_i)$.

Since our focus is the circumferential movement of the rivulet, only one section in the middle of the grid system is selected and analyzed. For a target circumferential section on the cable surface at the moment of t_i, its coordinates can be expressed by $\Omega(x_i, y_i, \theta_i, t_i)$, where x_i and y_i are Cartesian coordinates of the image plane, and θ_i is the circumferential position. As shown in Fig. 4(d), the cyan area is the identified upper rivulet, they are characterized by a group of scattered points $G(x_i, y_i, t_i)$. The white line that can be noticed in Fig. 4(d) is the mean value of circumferential position and is adopted to represent the upper rivulets. The blue line represents the grid curve of the target section $\Omega(x_i, y_i, \theta_i, t_i)$. Their intersection (the red spot) has the coordinates of $P(x_i, y_i, \theta_i, t_i)$, so the circumferential position θ_i of the upper rivulet at this moment (t_i) is recognized. By collecting serial positions of the upper rivulet at serial time t_i $(i = 1, 2, 3, \ldots\ldots)$, the circumferential movement of the upper rivulet is then obtained. The method for rivulet monitoring is similar to that of Li et al. (2015) and Jing et al. (2015) and the post processing philosophy is similar to Li et al. (2010b). However, unlike the experimental setup of Jing et al. (2015), in

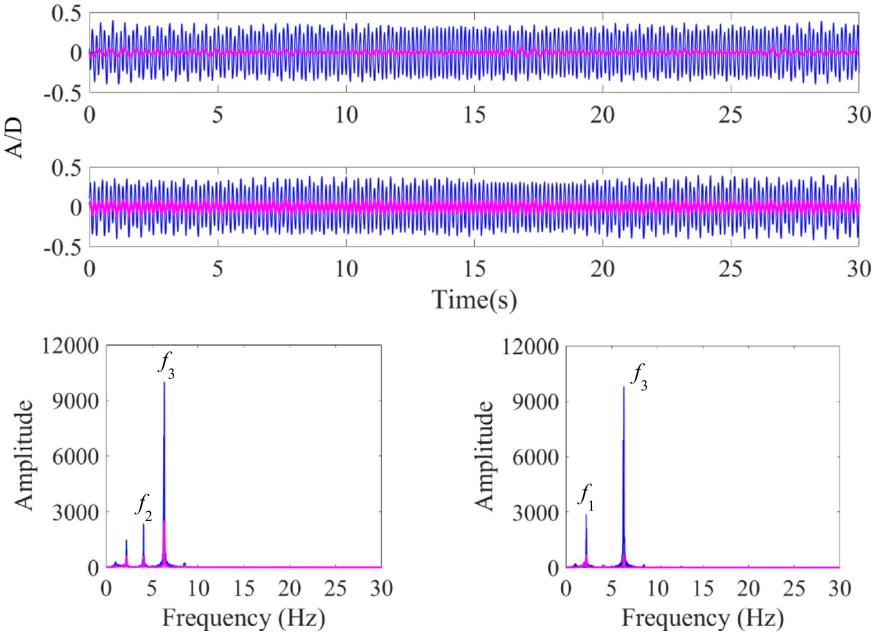

Fig. 9. The third mode displacement responses (up) and frequency spectrum (down) at $U = 14.60\ \mathrm{m{\cdot}s^{-1}}$, up-top: $L/2$; up-bottom: $L/6$; down-left: $L/2$; down-right: $L/6$. $f_1 = 2.21$ Hz, $f_2 = 4.09$ Hz, $f_3 = 6.33$ Hz. The blue lines denote the in-plane vibrations and the magenta lines denote the out-of-plane vibrations. (For interpretation of the references to color in this figure legend, the reader is referred to the web version of this article.)

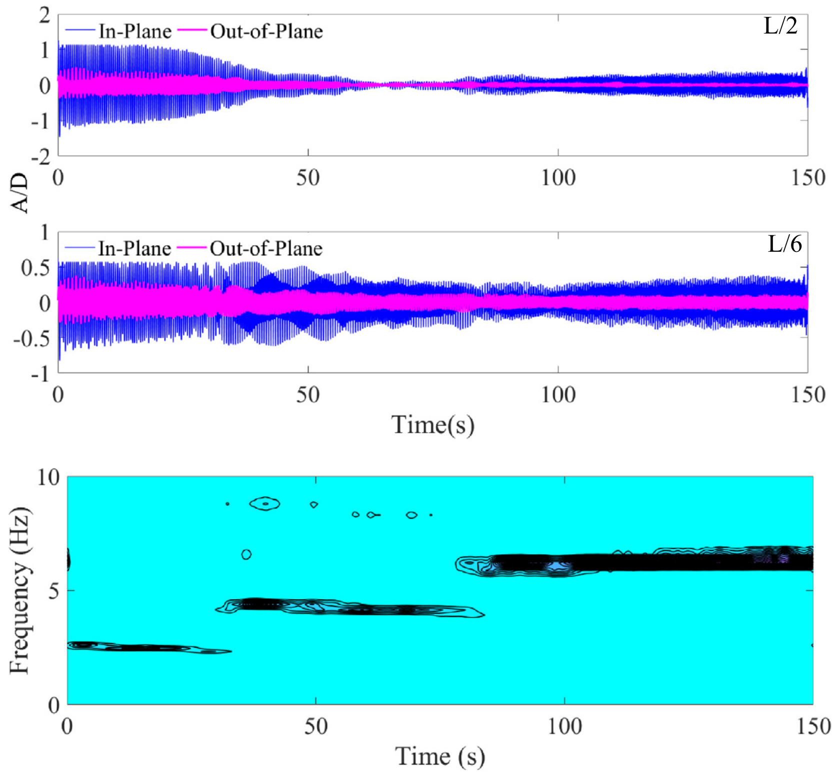

Fig. 10. Mode switch of the RWIV cable at $U = 14.60\ \mathrm{m{\cdot}s^{-1}}$, the vibration displacements measured at $L/2$ (top) and $L/6$ (middle), and time-frequency evolution of the cable vibration (bottom). In the displacement signals, the blue lines denote the in-plane vibrations and the magenta lines denote the out-of-plane vibrations. (For interpretation of the references to color in this figure legend, the reader is referred to the web version of this article.)

which the camera is fixed to the cable model and moved with it, the camera used in the present study is placed outside the wind tunnel.

2.3. PIV measurement

In addition to measurements of vibration responses and monitoring of upper rivulet, we also attempt to measure the flow structures around the flexible cable suffering from RWIVs. It is generally difficult to conduct PIV measurements in such a large wind tunnel. Tian et al. (2014) conducted a PIV measurement to investigate the effects of incoming wind conditions on the wake characteristics and dynamic wind loads acting on a wind turbine model. Their study is performed in a closed-loop wind tunnel with a test section of 2.4 m wide, 2.3 m high, and 20 m long. However, the test section employed in the present study is about 4 times theirs.

A high-resolution PIV system is adopted to conduct wake flow measurements around the cable model. The target plane is vertical and passing through the point which is 300 mm above the upper boundary of the rivulet monitoring region. Fig. 5 shows the experimental setup for PIV measurements. During PIV measurements, the incoming airflow is seeded with $\sim$1 μm oil droplets by using two droplet generators, which are placed on a corner of the smaller test section. The target plane is illuminated by a double-pulsed Nd:YAG laser adjusted on the second harmonic and emitting two pulses of 200 mJ at the wavelength of 532 nm with a repetition rate of 4 Hz. Manipulated by a set of optics and mirrors, the laser beam is shaped to a sheet with a thickness of about 1.0 mm in the target plane. A 16-bit CCD camera (PCO 1600, CookeCorp, resolution 1600 $\times$ 1200 pixels) is used for image acquisition with the axis of the camera being perpendicular to the laser sheet. The CCD camera and double-pulsed Nd:YAG lasers are connected to a host computer through a Digital Delay Generator (Berkeley Nucleonics, Model 575), which controls the timing of the laser illumination and the image acquisition. It should be noted that the CCD camera is fixed in the wake of the cable and inside the test section. Since the flexible cable is yawed at $\beta = 45°$, the interfering effects are expected to be negligible. Before the PIV tests, the neighboring region of the target plane is painted black to minimize the wall-laser noise. In addition, the test section is maintained completely dark by turning off the lights and curtaining off the windows with black clothes being glued on the outer surface of the glass tunnel walls during the PIV tests.

More than 500 frames of instantaneous PIV image pairs are obtained in order to ensure a good convergence of the measurements. After acquiring the PIV images, instantaneous velocity vectors are calculated by using frame to frame cross-correlation. The size of the interrogation window is 32 $\times$ 32 pixels and an effective overlap of 50% of the interrogation windows is employed in the PIV processing. After the instantaneous velocity vectors ($\boldsymbol{u}, \boldsymbol{v}$) being determined, the instantaneous spanwise vorticity ($\boldsymbol{\Omega}$) can be derived. The distributions of ensemble-averaged flow quantities, such as the mean velocity ($\overline{\boldsymbol{u}}$, $\overline{\boldsymbol{v}}$) and in-plane turbulence kinetic energy ($T.K.E = 0.5 \times (\boldsymbol{u}'^2 + \boldsymbol{v}'^2)/U^2$), can also be obtained from the instantaneous PIV measurements. For the PIV measurement conducted in the present study, the uncertainty level in the velocity measurement is estimated to be about 4.6%.

We investigated the incoming airflow speed in the range of U = 7.92–15.85 m·s^{-1}, with an increment of 0.42 m s^{-1}. During the experimental study, the inclination angle (α), the yaw angle (β) of the cable and the flow rate (Q) of the water supply were kept constant.

3. Experiment results

3.1. Multi-mode rain-wind induced vibrations of the flexible cable

The wind tunnel tests start at a wind speed U of 7.92 m s^{-1}. First, the upper water rivulet cannot be formed since it is found to drop or slip down to the lower surface of the cable model immediately after coming out from the water tube. As a result, the wind induced vibrations are found minimal and no RWIVs signal is recorded by the accelerometers. At the wind speed of 8.76 m s^{-1}, some water rivulets/film are found to climb up to the cable surface intermittently. However, no continuous upper rivulet is formed along the cable, thus no RWIVs vibration is observed. When the wind speed shifts from 10.01 m s^{-1} to 10.43 m s^{-1}, an upper rivulet is witnessed to form along the entire cable with periodical motion around the cable. The lower rivulet can also be noticed clearly but it remains almost static. At this wind speed, a large-amplitude cable RWIVs can be easily recognized by visual observation. From the mode shape of vibrations, it can be clearly identified that the RWIV vibrations in this case are mainly dominated by the first mode. As the wind speed increases, the amplitude of RWIVs is found to be gradually enhanced. At the wind speed of 13.76 m s^{-1}, the RWIV amplitudes are observed to be strikingly large. As the wind speed changes from 13.76 m s^{-1} to 14.18 m s^{-1}, the vibration amplitudes are decreased but still notable. It should be noted that, in this case, the mode shape suggests that the cable vibration is dominated by the second mode, as the shape node is nearly fixed at $L/2$. When the wind speed increases to 14.60 m s^{-1}, the dominated vibration mode changes to its third mode, as will be revealed by frequency analysis. After that, the cable remains to vibrate with its third mode with the wind speed increasing up to 15.85 m s^{-1}.

Fig. 6(a) illustrates the all-time root-mean-square (RMS) values of the vibration displacements of the flexible cable measured at $L/2$ and $L/6$. The vibration amplitudes (A) are obtained by integrating the acceleration signals and then non-dimensionalized by the diameter of the cable ($D = 98.36$ mm). The vibration frequencies are also identified by performing Fast Fourier Transform (FFT) analysis to plot Fig. 6(b). It can be seen from Fig. 6(a) that the cable vibration responses are very

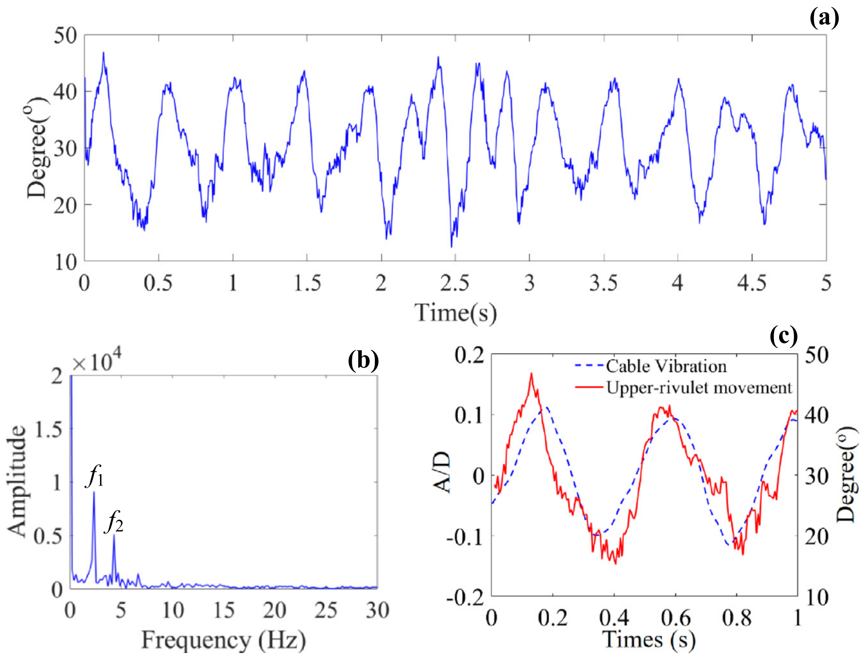

Fig. 11. The first-mode frequency dominated oscillation of the upper rivulet during RWIV at $U = 11.26$ m·s^{-1}. (a) Oscillation of the upper rivulet; (b) Frequency spectrum of the rivulet movement; (c) Comparison of the upper rivulet movement and cable vibration.

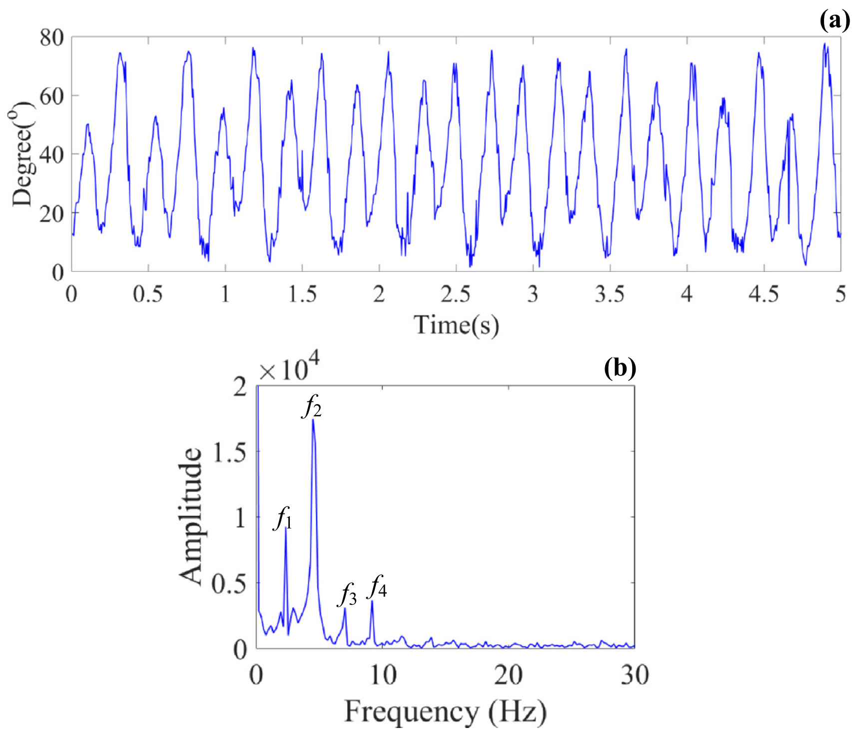

Fig. 12. The second-mode frequency dominated oscillation of the upper rivulet during RWIV at $U = 14.18$ m·s^{-1}. (a) Oscillation of the upper rivulet; (b) Frequency spectrum of the rivulet movement.

small at lower wind speeds. However, as the wind speed increases from 10.01 m s^{-1} to 10.43 m s^{-1}, the in-plane vibration amplitudes witness a sudden increase due to the occurrence of RWIVs. As the wind speed increases, RWIVs continue to develop, and the in-plane vibration amplitudes become larger. Meanwhile, the out-of-plane cable vibrations are consistently

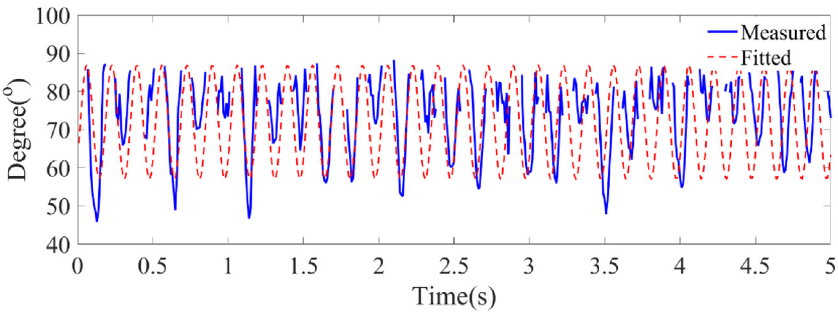

Fig. 13. The third-mode frequency dominated oscillation of the upper rivulet in the occurrence of RWIV at U= 14.60 m·s^{-1}. The discontinuous blue lines denote the identified positions and the dashed red line denotes the fitted curve with a sinusoidal function. Frequency of the fitted sine wave is 6.047 Hz. (For interpretation of the references to color in this figure legend, the reader is referred to the web version of this article.)

smaller in comparison with the in-plane vibration responses. It could also be noted that, in the wind speed range 14.18–14.60 m·s^{-1}, the amplitudes of cable vibrations witness a divergence, because a *mode switch* phenomenon is observed. As shown in Fig. 6(b), when the wind speed is below 14.18 m s^{-1}, the cable vibration is dominated by its first mode frequency. As the cable vibrations shift from the first mode to the second, the vibration amplitudes measured at $L/2$ experience a sudden and remarkable drop, as can be observed in Fig. 6(a). As the incoming wind speed continues to increase to 14.60 m s^{-1}, the first, second, or third mode vibrations can be observed from the cable vibration signals, even though the test conditions are remained exactly the same. When the incoming wind speed exceeds 14.60 m s^{-1}, the cable vibrations are dominated by the third-mode frequency. In the present study, three different test cases, i.e., at the wind speeds of 11.26, 14.18 and 14.60 m s^{-1} are selected to present and analyze the structural responses of the first, second and third mode RWIVs respectively.

The displacement responses of the flexible cable suffering from RWIVs at the incoming wind U of 11.26 m s^{-1} are calculated and presented in Fig. 7. Typical RWIVs maintain within a period of 30 s and the in-plane vibration amplitudes measured at $L/2$ and $L/6$ are both larger than those of the out-of-plane amplitudes. It can also be noticed that the vibration amplitudes measured at $L/6$ are smaller than $L/2$, which agrees with the first-mode behaviors. In addition, the maximum in-plane vibration amplitude measured at $L/2$ is about 1.1 times the cable diameter. The frequency spectra of the cable vibrations are also identified by FFT and illustrated in Fig. 7. Clearly, the RWIVs in this case are mainly dominated by its first mode, and the second mode is also found to participate with a lower peak.

Ni et al. (2007) observed that the vibrations with higher modes tend to occur at a higher wind speed even with the same attack angle, during their continuous 45-day field measurements conducted on the Dongting Lake cable-stayed Bridge. In the present study, a similar phenomenon is observed. In the wind tunnel tests, all the conditions are remained constant, including the water supply, the inclination angle and the yawed angle of the cable model. When the wind speed is increased to $U = 14.18$ m s^{-1}, the second-mode dominated RWIVs gradually develop. The displacement responses of the flexible cable suffering from RWIVs in this case are illustrated in Fig. 8. In the mid span, the cable vibrations are less prominent because the accelerometers are close to the node of the second-mode cable vibration. At the $L/6$ knot, the in-plane vibration amplitudes are larger than the out-of-plane amplitudes, which is similar to the first-mode RWIVs discussed above. Besides, the maximum in-plane vibration amplitude measured at $L/6$ is (0.3–0.45) times the cable diameter. The frequency spectra of the cable vibrations are also presented in Fig. 8. The first four modes are found to participate in the RWIVs in this case and are mainly dominated by its second one.

When the wind speed U is increased to 14.60 m s^{-1}, the third-mode dominated RWIVs take place. The vibration responses of the flexible cable suffering from third-mode RWIV and the frequency spectrum in this case are plotted in Fig. 9. The first three modes are found to participate in the RWIVs at this wind speed and the cable vibrations are mainly dominated by its third-mode. It can be concluded that the multi-mode RWIVs often involves participation of a dominant mode as well as other modes. In addition, the higher-mode RWIVs tend to occur at higher wind speed. As the wind speed approaches higher, the frequency of the vortex shedding from the cable becomes larger and synchronizes with higher-mode cable frequencies. These characteristics of rain-wind induced vibrations are similar to those of the multi-mode vortex induced vibrations.

Similar to what happened at the wind speed of $U = 14.18$ m s^{-1}, the third-mode dominated RWIVs with $U = 14.60$ m s^{-1} are found to switch to the second and first modes, or vice versa. This phenomenon, i.e., different modes occur at the same incoming wind speed, is called mode switch. In Violette et al. (2010), vortex induced vibration was investigated by formulating a theoretical model. Possible overlaps of reduced velocity ranges of instability were predicted between adjacent modes. The mode switch phenomenon observed in the present study is illustrated in Fig. 10 . It can be seen that the RWIVs of the flexible cable experience the first, second and third-mode respectively within 150 s at $U = 14.60$ m s^{-1}.

3.2. Upper-rivulet dynamics

As the wind speed increases to $U = 11.26$ m s^{-1}, the first mode RWIVs develop. Fig. 11(a) illustrates the averaged movement of the upper rivulet in this case. The averaged position of upper rivulet is calculated to be 52.4° with a standard deviation of 7.28°. Li et al. (2010a) reported that the upper rivulet oscillated around the equilibrium position of 66° with a deviation of 7.01°. Besides, during the experiments of Li et al. (2015) and Jing et al. (2015), the averaged rivulet position oscillated with an equilibrium position at 63° (by definition of the present study) and a standard deviation of 6.37°. The diameter of cable model adopted by Li et al. (2010a) is 100 mm, which is very close to the present one, so the standard deviations of rivulet oscillation are found close.

The frequency components of the rivulet dynamics are identified by using a Fast Fourier Transform (FFT) analysis and the result is presented in Fig. 11(b). It can be seen that the rivulet movement is dominated by the first and second mode frequencies, which are the same as the vibration frequencies of the flexible cable. The phenomenon of frequency resonance is consistent with previous experiment tests (Li et al., 2010a; Jing et al., 2015; Li et al., 2015) and numerical studies (Bi et al., 2013, 2014; Wang et al., 2016). In addition, the movement of averaged upper rivulet within 1 s is compared with the cable vibration, as shown in Fig. 11(c). It can be observed that when the cable moves upward, the upper rivulet shifts to the leeward surface (i.e., the angle becomes smaller). Conversely, when the cable moves downward, the rivulet moves upwind. As a result, the rivulet oscillation and the cable vibration are roughly in-phase, though a slight phase lag can be noted. The similar phenomenon has also been observed by Cosentino et al. (2003a) and Jing et al. (2017).

When the wind speed is increased to U =14.18 m s^{-1}, the second-mode dominated RWIV takes place. Fig. 12(a) illustrates the averaged movement of the upper rivulet in this case. The averaged position of upper rivulet is calculated to be 57.6° and its standard deviation 19.8°. The oscillation frequency of the rivulet movement is identified by using a FFT analysis and the result is presented in Fig. 12(b). It can be seen that the rivulet movement is dominated by the same frequency as the frequency spectrum the cable vibrations: the second mode frequency. The phenomenon of frequency resonance is consistent with what occurred for the first mode RWIVs at smaller incoming wind speed U.

The flexible cable will experience the third-mode frequency dominated RWIVs when the incoming wind speed reaches U = 14.60 m s^{-1}. In this case, the difficulty of image recording and processing increases and causes the discontinuity of the movement signal of upper rivulet, as shown in the blue lines in Fig. 13. However, we fitted the discontinuous signals by using a sinusoidal function with the third mode frequency of the cable vibration. As the red dashed curve illustrated in Fig. 13, the frequency of the fitted sine wave is 6.047 Hz. Though the identified upper rivulet signal is not as clean as those obtained in the first and second mode RWIVs, Fig. 13 still carries some serious weight of the present study: (1) the upper rivulet movement is dominated by the third mode frequency, which is close the cable vibration; (2) The phenomenon of higher-mode frequency resonance is consistent with what is also observed in the first and second mode RWIVs; (3) both the averaged position and the standard deviation of the upper rivulet oscillation are significantly larger than their counterparts of the first and second mode RWIVs.

It is also interesting to note that the RWIVs of the cable could be developed into a *steady* state. In this case, the upper rivulet is found nearly static and exhibits no periodicity during the experiments. Fig. 14 shows the time history and frequency spectrum of the cable vibrations. It can be seen that the vibration amplitudes are steady. The average position of the upper rivulet in this case is identified as 61.6° with a small standard deviation of 0.28°, as shown in Fig. 14(c). The FFT analysis of the upper rivulet movement is plotted in Fig. 14(d). Obviously, the rivulet movement shows no periodicity. It should be noted that, in most cases of RWIVs, the upper rivulet oscillates periodically with a close frequency to the cable vibrations. This is consistent with the conventional viewpoint. This case presented in Fig. 14 is the only one exception and we failed to reproduce it for a second time, even under the same wind and rain conditions. However, this exceptional case did occur and is recorded. We present it here because it might contribute to improving the understanding the theory of artificial rivulet. It is also worth noting that, though we name this case steady RWIVs, we do not imply that the others are *unsteady*. By using an analytical model, Xu and Wang (2003) predicted the dynamic behavior of a circular cylinder with a fixed rivulet. It is shown that, with a small given initial displacement, the vibration amplitude of the cylinder gradually increased with time. However, the motion of the cylinder is found to be periodic with a nearly constant amplitude after a certain computation period (320 s). Their simulation results suggested that even a fixed rivulet would possibly generate, or at least maintain a steady RWIV, if a small initial cable displacement is imposed. In the case presented in Fig. 14, RWIVs develop into a steady state and the upper rivulet is found nearly fixed, which is very much similar to the steady state of their calculation. Previous studies (see Xu and Wang, 2003; Xu et al., 2006; Gu and Huang, 2008; Gu, 2009; Du et al., 2013) have shown that the theoretical models based on the assumption of fixed artificial rivulet work well in predicting the steady amplitude of RWIV, and the exceptional case of the present study provides an experimental evidence for their analytical models.

3.3. Flow structures obtained by PIV measurement

During the PIV measurements, the incoming airflow is seeded with ∼1 μm oil droplets generated by two droplet generators. The seeding density is found to be adequate for interrogation windows of size 32 × 32 pixels. Samimy and Lele (1991) proposed that the particle response could be well characterized by ζ, the ratio of particle response time (ζ_p) to the flow time scale (ζ_f), and only particles with $\zeta < 0.05$ are able to represent the flow features. This is indeed the case in the present PIV measurement, where $\zeta = \zeta_p/\zeta_f = 1.77 \times 10^{-3}$. In addition, we calculated the uncertainty of the PIV measurement used in the present study. By using the method proposed by Park et al. (2008), the uncertainty level for the present study in the velocity measurement is estimated to be about 4.6%. We adopted the conception of swirling strength to visualize the vortex motion behind the cable model, to eliminate the influences of the strong shear-layer motion in the

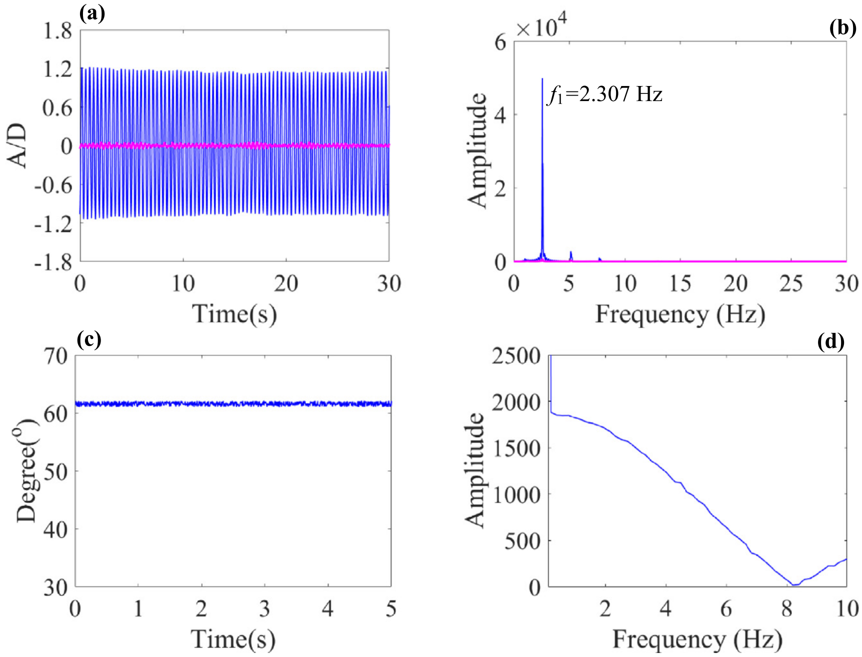

Fig. 14. Dynamics of upper rivulet when the cable model is suffering from a steady RWIV at U= 11.26 m/s. (a) Displacements of steady RWIV; (b) Frequency spectrum of steady RWIV vibrations; (c) Movement of the upper rivulet; (d) Frequency spectrum of the rivulet movement. *It should be especially noted that this unique case has never been observed or recorded for a second time in the wind tunnel tests.

near-wall on the rotation motions. Swirling strength is defined by Zhou et al. (1999) as the imaginary part of the complex eigenvalues of the velocity gradient tensor, it reads

$$D_{2-D} = \begin{bmatrix} \frac{\partial \boldsymbol{u}}{\partial x} & \frac{\partial \boldsymbol{u}}{\partial y} \\ \frac{\partial \boldsymbol{v}}{\partial x} & \frac{\partial \boldsymbol{v}}{\partial y} \end{bmatrix}$$

Fig. 15 presents the evolution of the wake flow structures behind the dry cable at $U = 11.26\ \mathrm{m\ s^{-1}}$. The vibrations of the dry cable are minimal in this case. The regular vortex shedding process can be clearly identified. It can also be noted that the vortex structures are not perfectly symmetric, which is due to the inclination and yawing of the cable set-up in the wind tunnel. Nevertheless, the von Kármán vortex structure from the cable remains complete, and is found to shed periodically.

Fig. 16 shows the flow when the cable is suffering from RWIVs at $U = 11.26\ \mathrm{m\ s^{-1}}$. It can be seen that the wake flow structures become more disordered, the overall vortex strength is increased, and the vortex formation length shrinks, in comparison with the flow around a dry cable. This indicates a good agreement with the experimental results reported by Alam and Zhou (2007). Fig. 16 also implies that the existence and oscillation of the upper rivulet could impair the two-dimensionality of the wake flow. In comparison with the wake flow of the dry cable, the wake flow structures in this case have obviously been influenced by some small-scale vortices, since the flow structures become more disordered and discrete. Possible origin of the small-scale vortices is the boundary-layer instability, due to the existence, oscillation and disturbance of upper water rivulet.

4. Discussion

4.1. RWIVs from the perspective of VIVs

From the experiments, two notable phenomena have been observed: the first, second and third mode dominated RWIVs take place successively with the increase of wind speed; two or three adjacent modes have a chance to overlap (mode switch) for a particular wind speed (at $U = 14.18\ \mathrm{m\ s^{-1}}$ and $U = 14.60\ \mathrm{m\ s^{-1}}$). These observations are similar to the coupled-wake flutter (CWF, see De Langre, 2006; Violette et al., 2010) mechanism usually observed in vortex induced vibrations (VIVs) of flexible structures. In the article of Matsumoto et al. (2003a), RWIV was explained as a vortex-induced vibration, but at high reduced wind velocity. In their wind tunnel tests, they found two dominant frequencies: one is linked to von Kármán vortex shedding and the other is at a much lower frequency. The latter one is considered to be the driven force of RWIV. Besides,

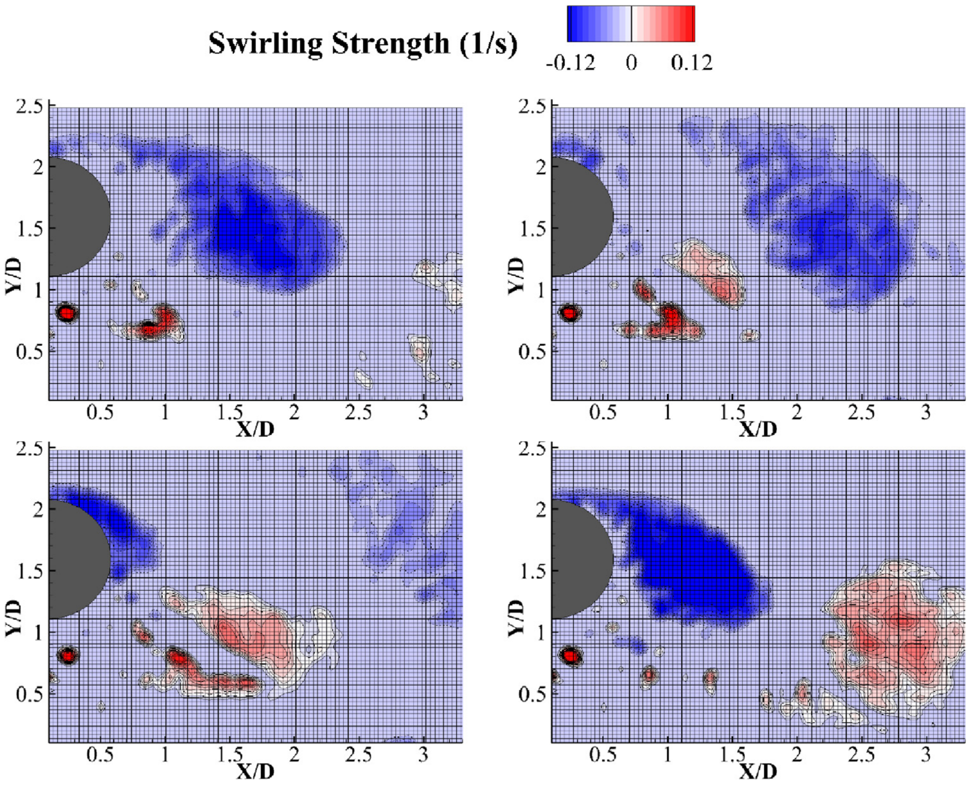

Fig. 15. Wake flow evolution of the dry cable at U=11.26 m·s^{-1}.

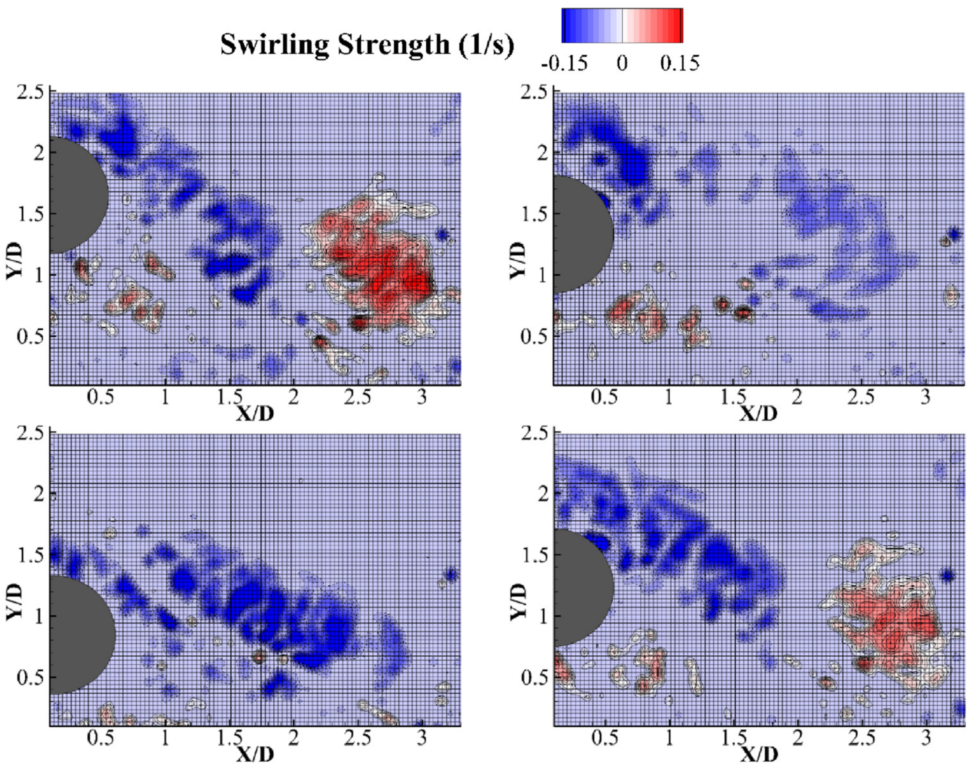

Fig. 16. Wake flow evolution of the RWIV cable at U=11.26 m·s^{-1}.

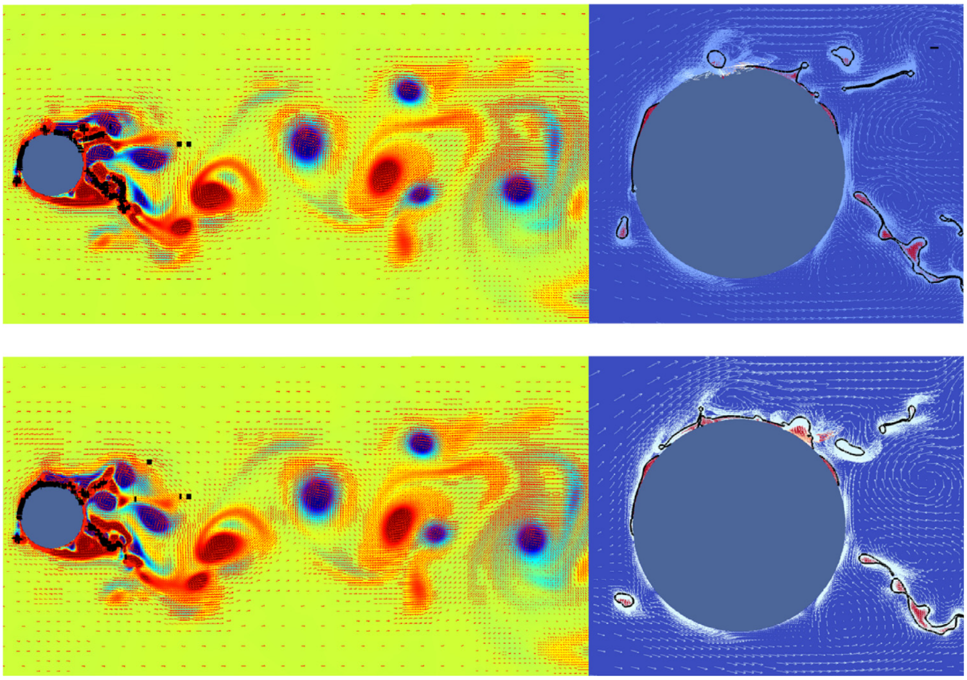

Fig. 17. Flow around a circular cylinder with water rivulet (left) and the magnified view of the detachment flow (top right) and reattachment flow (bottom right) near the rivulet carpet (Cheng, 2015). * With the permission to reprint from Peng Cheng.

Table 2
Low frequency components reported in previous studies.

Contributors	Approach	Frequency (Hz)	Diameter (m)	*U* (m/s)	*St*
Chen et al. (2013)	Numerical	0.946–1.526	0.1	7.50	0.0126–0.0203
Cheng et al. (2015)	Numerical	0.9765	0.1	7.72	0.0126
Bi et al. (2014)	Numerical	0.889	0.1	7.72	0.0115
Wang et al. (2016)	Numerical	1.0	0.1	7.72	0.0130
Matsumoto et al. (2003a)	Experimental	0.4486	0.054	6.0	0.0125

substantial similarity between VIVs and RWIVs are observed in the *in-situ* field monitoring results reported by Zuo et al. (2008). It is suggested that the RWIV might be due to a different vortex-induced type of excitation from the conventional von Kármán vortex shedding.

Table 2 reviews some recent results on the dominant frequencies in the lift forces during RWIVs. It is shown that the value of Strouhal number (*St*) is about 0.012, while the *St* is usually much larger (0.16–0.25) for the conventional von Kármán vortex shedding from a dry cable. This may indicate a great modification of the vortex shedding in the near wake. It has been suggested that RWIVs may be excited by another type of vortex shedding, with much lower frequency components. From the perspective of VIVs, the cable vibrations can be explained as the coupled-wake flutter (CWF, De Langre, 2006; Violette et al., 2010). Regarding the coupled two modes of the RWIV system, i.e., the structure mode and the wake mode, the structure part is clean and clear, thus the key to understand this problem must be hidden in the wake mode.

4.2. Bubble burst as a possible cause

As reviewed in the introduction, considerable research efforts have been devoted to stall, most of the previous studies, however, focused on stall of airfoils. The stall over a circular cylinder has rarely been studied in detail. Nevertheless, some researchers did report findings closely related to stall of a circular cylinder though they have not been linked to stall yet. In Matsumoto et al. (2003b), they experimentally investigated the aerodynamic behaviors of a circular cylinder with an artificial rivulet. The low frequency components in the lift force were recorded and identified. They related the low frequency components to the excitation of RWIV and explained it as a type of vortex-induced vibration at high reduced wind velocities. More recently, Cheng (2015) combined direct numerical simulations (DNS) and large eddy simulations (LES) to address the physical process of real rain droplets falling onto the cable surface subject to the incoming wind. Fig. 17 reprints the vortex shedding process and flow topology around the circular cylinder observed by Cheng (2015). Diameter of the circular cylinder is 0.1 m and the incoming wind speed is 7.72 m s^{-1}. Two types of flow topologies over the cylinder surface, i.e., a long bubble

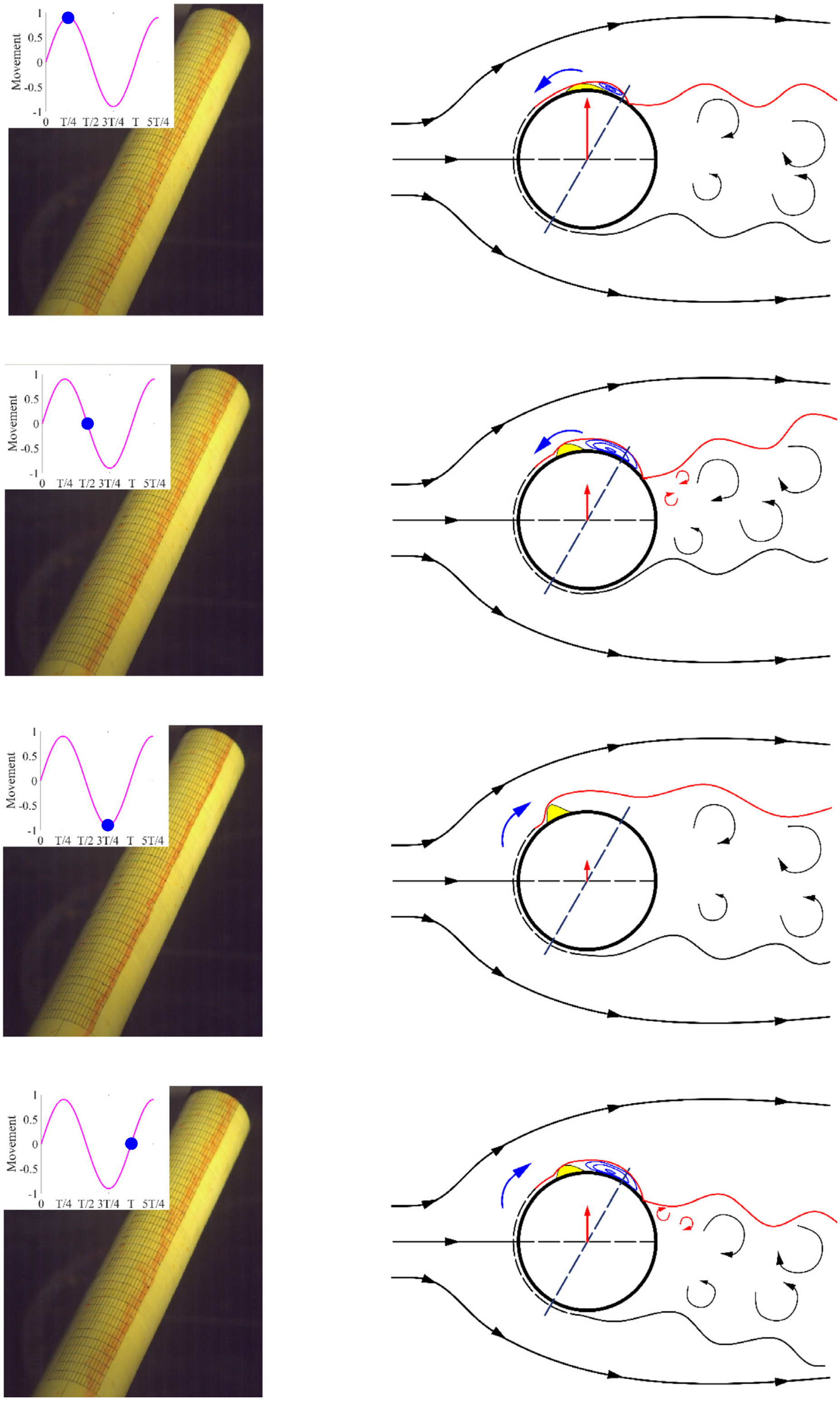

Fig. 18. Water film evolution on the cable model surface (left) and sketch of the bubble flow around the cable model (right). The blue arrows donate the evolution tendency of the rivulet, the straight red arrows donate the relative scale of lift forces acting on the cable, and the curved red arrows denote the small-scaled vortices originated from bubble burst. (For interpretation of the references to color in this figure legend, the reader is referred to the web version of this article.)

(detachment flow) and a short bubble (reattachment flow) behind the water rivulet can be observed, as shown in Fig. 17. It should also be mentioned that he identified the dominant frequency in the time history of lift force to be 2.59 Hz. For a regular and smooth circular cylinder, the Strouhal number at this Re level is about 0.20 and the resultant von Kármán vortex shedding frequency is estimated to be $f_v = StU/D = 15.48$ Hz. Therefore, the bubble burst from short bubble to long bubble results in a substantial frequency decrease, which is one of the characteristics of stall. In addition, a notable and sudden drop and gradual recovery of the lift force are observed (see Fig. 5.20(b) of Cheng (2015). The sharp drop and gradual recovery of lift force and the dramatic decrease of frequency, which are strongly linked to the transitional process of bubble burst, exhibit similarities with the stall phenomenon over airfoils. Moreover, we can notice in Fig. 17 that the alternating structures of von Kármán vortex are alleviated by the small-scaled vortices, especially within the very near wake behind the circular cylinder. This is also supported by one of the characteristics of stall, as we concluded above. This modification on von Kármán vortex shedding might be due to the Kelvin–Helmholtz vortices generated from the separation layers. Alam and Zhou (2007) investigated experimentally the fluid structures around a circular cylinder with water rivulet running on the surface. They observed the small-scaled Kelvin–Helmholtz vortices in the separating shear layer. It was proposed by Alam and Zhou (2007) that the oscillation of the water rivulet could result in Kelvin–Helmholtz vortices of lower frequency. In our PIV measurement results shown in Fig. 16, the von Kármán vortex shedding is alleviated and the small-scaled flow structures are developed with the formation and oscillation of upper rivulet.

The scenario we propose is as follows. When the cable model is at its highest position, the water film is spread out like a water carpet, in this case the reattachment (short) bubble is formed behind the water film, as sketched in Fig. 18. As the cable moves downward (descending), the water film tends to gather. At the same time, the separation flow near the upper rivulet tends to move away from the cable centerline, while the separation flow near the lower rivulet tends to approach the cable centerline. As a result, the separation bubble formed behind the upper rivulet is gradually elongated and eventually destroyed. As a consequence, a bubble burst occurs. Some small-scaled vortices generated in the boundary layer could contribute to alleviating the von Kármán vortex shedding and generating low frequency components. Finally, the rivulet gathers as a thick hump, the flow reattachment is completely destroyed and the separation–type flow (long bubble) is formed near the upper rivulet, as the cable vibration reaches its lowest position. When the cable moves upward (ascending), the gathered hump of water rivulet tends to spread out as a carpet and the separation flow near the upper rivulet points at the cable centerline. In consequence, the reattachment bubble flow (short bubble) is gradually formed again. The bubble flow results in a large lift force, due to the asymmetry of flow and pressure distribution (Jing et al., 2017). It can be concluded that the bubble burst will lead to a sudden and significant decrease of lift force acting on the cable as the cable moves downward. In contrast, a large lift force will be generated as the bubble reattachment is formed and developed as the cable moves upward. It can be seen that the change of lift force always contributes to promoting the cable vibrations (Fig. 18).

Based on the discussion above, bubble burst as a possible excitation mechanism of RWIVs can be described as: vibration of the cable (even with a very small amplitude) drives the movement of separation point (Lemaitre et al., 2007; Mei and Currie, 1969), the movement of separation points and angle of separation will change the shear layer trajectory. During this, a bubble burst resulted from Kelvin–Helmholtz instability would take place (Rinoie and Takemura, 2004), and the stall phenomenon occur. As a result, the von Kármán vortex shedding is mitigated and the vortex shedding frequency witness a sudden and substantial decrease (Cheng, 2015; Zaman et al., 1989; Alam and Sandham, 2000; Rinoie and Takemura, 2004). The vortex shedding with decreased frequency is then synchronized with the cable's structure frequency, resulting in a larger vibration amplitude. In the second loop, a larger cable amplitude could inverse enhance the traveling of the separation point (Mei and Currie, 1969). Consequently, the RWIVs with very large amplitudes could be developed rapidly, as we observed in the wind tunnel experiments.

5. Conclusion

In this paper, we addressed the dynamics of upper rivulet, the flow structures and a possible excitation mechanism of the cable suffering from RWIVs. Some conclusions can be drawn:

(1) It is feasible to reproduce multi-mode RWIVs in a wind tunnel. Higher mode RWIVs tend to develop at higher wind speeds and the mode switch phenomenon can be observed at some particular wind speeds. These characteristics of multi-mode RWIVs exhibit substantial similarities to VIVs.

(2) During the RWIVs, the oscillation frequency of the upper rivulet is synchronized with the cable vibration frequency. This phenomenon is observed in the first, second and third mode RWIVs. In addition, we report an exceptional case in the present paper, i.e., when the cable is experiencing steady RWIV, the upper rivulet is nearly fixed on the cable surface and exhibits no periodicity.

(3) By employing PIV, the regular von Kármán vortex shedding is clearly identified in the wake of the dry cable. However, when the cable is suffering from RWIVs, the wake flow structures become more disordered, the vortex strength is increased, and the vortex formation length shrinks, due to the existence and oscillation of the upper rivulet. The von Kármán vortex shedding is alleviated and the small-scaled vortical structures become more present, with the formation and oscillation of upper rivulet.

(4) A new excitation mechanism of RWIVs (i.e., bubble burst) is proposed. In this scenario, the vibration of the cable drives the movement of separation point and the upper rivulet. The movement of upper rivulet result in a bubble burst and a stall phenomenon due to the Kelvin–Helmholtz instability in the boundary layer. As a consequence, the von Kármán vortex shedding can be alleviated and the vortex shedding frequency substantially decreased. As the decreased vortex shedding synchronize with the cable's structure frequency, large-amplitude RWIVs develop.

Acknowledgments

This study is funded by the National Key Research and Development Program of China (2016YFC0701107), National Natural Science Foundation of China (NSFC, No. 51378153, 51578188 and 51722805) and the Fundamental Research Funds for the Central Universities (HIT. BRETIV. 201803 and HIT. BRETIII. 201512). D. G. also acknowledges the financial support from China Scholarship Council (CSC 201606120189).

References

Achenbach, E., 1968. Distribution of local pressure and skin friction around a circular cylinder in cross-flow up to Re $= 5 \times 10^6$. J. Fluid Mech. 34 (4), 625–639.
Alam, M., Sandham, N.D., 2000. Direct numerical simulation of short laminar separation bubbles with turbulent reattachment. J. Fluid Mech. 410, 1–28.
Alam, M.M., Zhou, Y., 2007. Turbulent wake of an inclined cylinder with water running. J. Fluid Mech. 589, 261–03.
Bi, J., Lu, P., Wang, J., Bao, C., Guan, J., 2014. Numerical simulation and analysis of the effects of water-film morphological changes on the aerodynamic lift of stay cables. J. Fluids Struct. 48 (Suppl. C), 376–392.
Bi, J., Wang, J., Shao, Q., Lu, P., Guan, J., Li, Q., 2013. 2D numerical analysis on evolution of water film and cable vibration response subject to wind and rain. J. Wind Eng. Ind. Aerodyn. 121 (Suppl. C), 49–59.
Chen, W.L., Tang, S.R., Li, H., Hu, H., 2013. Influence of dynamic properties and position of rivulet on rain–wind-induced vibration of stay cables. J. Bridge Eng. 18 (10), 1021–1031.
Cheng, P., 2015. Numerical Simulations for Rain-Wind-Induced Vibration (Ph.D. thesis). Université Pierre et Marie Curie-Paris VI.
Cheng, P., Li, H., Fuster, D., Chen, W., Zaleski, S., 2015. Multi-scale simulation of rainwater morphology evolution on a cylinder subjected to wind. Comput. & Fluids 123, 112–121.
Cosentino, N., Flamand, O., Ceccoli, C., 2003. Rain-wind induced vibration of inclined stay cables-Part I: Experimental investigation and physical explanation. Wind Struct. 6 (6), 471–484.
Cosentino, N., Flamand, O., Ceccoli, C., 2003. Rain-wind induced vibration of inclined stay cables-Part II: Mechanical modeling and parameter characterisation. Wind Struct. 6 (6), 485–498.
De Langre, E., 2006. Frequency lock-in is caused by coupled-mode flutter. J. Fluids Struct. 22 (6), 783–791.
Du, X., Gu, M., Chen, S., 2013. Aerodynamic characteristics of an inclined and yawed circular cylinder with artificial rivulet. J. Fluids Struct. 43, 64–82.
Geurts, C., Vrouwenvelder, T., van Staalduinen, P., Reusink, J., 1998. Numerical modelling of rain-wind-induced vibration: Erasmus Bridge, Rotterdam. Struct. Eng. Int. 8 (2), 129–135.
Gu, M., 2009. On wind-rain induced vibration of cables of cable-stayed bridges based on quasi-steady assumption. J. Wind Eng. Ind. Aerodyn. 97 (7), 381–391. 12th International Conference on Wind Engineering.
Gu, M., Huang, L., 2008. Theoretical and experimental studies on the aerodynamic instability of a two-dimensional circular cylinder with a moving attachment. J. Fluids Struct. 24 (2), 200–211.
Hikami, Y., Shiraishi, N., 1988. Rain-wind induced vibrations of cables stayed bridges. J. Wind Eng. Ind. Aerodyn. 29 (1), 409–418.
Jing, H., He, X., Li, H., 2018. Initial condition and damping effects on rain- wind induced cable vibration. J. Wind Eng. Ind. Aerodyn. 175, 376–383.
Jing, H., Xia, Y., Li, H., Xu, Y., Li, Y., 2015. Study on the role of rivulet in rain-wind-induced cable vibration through wind tunnel testing. J. Fluids Struct. 59 (Suppl. C), 316–327.
Jing, H., Xia, Y., Li, H., Xu, Y., Li, Y., 2017. Excitation mechanism of rain-wind induced cable vibration in a wind tunnel. J. Fluids Struct. 68 (Suppl. C), 32–47.
Lemaitre, C., De Langre, E., Hémon, P., 2010. Rainwater rivulets running on a stay cable subject to wind. Eur. J. Mech. B Fluids 29 (4), 251–258.
Lemaitre, C., Hémon, P., de Langre, E., 2007. Thin water film around a cable subject to wind. J. Wind Eng. Ind. Aerodyn. 95 (9), 1259–1271.
Li, F.C., Chen, W.L., Li, H., Zhang, R., 2010. An ultrasonic transmission thickness measurement system for study of water rivulets characteristics of stay cables suffering from wind-rain-induced vibration. Sensors Actuators A 159 (1), 12–23.
Li, H., Chen, W.L., Xu, F., Li, F.C., Ou, J.P., 2010. A numerical and experimental hybrid approach for the investigation of aerodynamic forces on stay cables suffering from rain-wind induced vibration. J. Fluids Struct. 26 (7), 1195–1215.
Li, Y., Jing, H., Xia, Y., Xu, Y., Xiang, H., 2015. Measurement of rivulet movement on inclined cables during rain-wind induced vibration. Sensors Actuators A 230 (Suppl. C), 17–24.
Matsumoto, M., 1989. Wind-induced cable vibration of cable-stayed bridges. In: Proc. of Japan-Canada Joint Workshop on Bridge Aerodynamics, pp. 101–110.
Matsumoto, M., Shirato, H., Yagi, T., Goto, M., Sakai, S., Ohya, J., 2003. Field observation of the full-scale wind-induced cable vibration. J. Wind Eng. Ind. Aerodyn. 91 (1), 13–26.
Matsumoto, M., Yagi, T., Goto, M., Sakai, S., 2003. Rain-wind-induced vibration of inclined cables at limited high reduced wind velocity region. J. Wind Eng. Ind. Aerodyn. 91 (1), 1–12.
Matsumoto, M., Yagi, T., Sakai, S., Ohya, J., Okada, T., 2005. Steady wind force coefficients of inclined stay cables with water rivulet and their application to aerodynamics. Wind Struct. 8 (2), 107–120.
Mei, V.C., Currie, I., 1969. Flow separation on a vibrating circular cylinder. Phys. Fluids 12 (11), 2248–2254.
Ni, Y., Wang, X., Chen, Z., Ko, J., 2007. Field observations of rain-wind-induced cable vibration in cable-stayed dongting lake bridge. J. Wind Eng. Ind. Aerodyn. 95 (5), 303–328.
Park, J., Derrandji-Aouat, A., Wu, B., Nishio, S., Jacquin, E., 2008. Uncertainty analysis: particle imaging velocimetry. In: ITTC Recommended Procedures and Guidelines, International Towing Tank Conference.
Rinoie, K., Takemura, N., 2004. Oscillating behaviour of laminar separation bubble formed on an aerofoil near stall. Aeronaut. J. (1968) 108 (1081), 153–163.
Robertson, A., Taylor, I., Wilson, S., Duffy, B., Sullivan, J., 2010. Numerical simulation of rivulet evolution on a horizontal cable subject to an external aerodynamic field. J. Fluids Struct. 26 (1), 50–73.
Samimy, M., Lele, S., 1991. Motion of particles with inertia in a compressible free shear layer. Phys. Fluids A 3 (8), 1915–1923.
Taylor, I.J., Robertson, A.C., 2011. Numerical simulation of the airflow-rivulet interaction associated with the rain-wind induced vibration phenomenon. J. Wind Eng. Ind. Aerodyn. 99 (9), 931–944.
Tian, W., Ozbay, A., Hu, H., 2014. Effects of incoming surface wind conditions on the wake characteristics and dynamic wind loads acting on a wind turbine model. Phys. Fluids 26 (12), 125108.
Violette, R., de Langre, E., Szydlowski, J., 2010. A linear stability approach to vortex-induced vibrations and waves. J. Fluids Struct. 26 (3), 442–466.
Wang, J., Lu, P., Bi, J., Guan, J., Qiao, H., 2016. Three-phase coupled modelling research on rain-wind induced vibration of stay cable based on lubrication theory. J. Fluids Struct. 63 (Suppl. C), 16–39.
Wang, Z., Zhou, Y., Huang, J., Xu, Y., 2005. Fluid dynamics around an inclined cylinder with running water rivulets. J. Fluids Struct. 21 (1), 49–64.

Xu, Y., Wang, L., 2003. Analytical study of wind-rain-induced cable vibration: SDOF model. J. Wind Eng. Ind. Aerodyn. 91 (1), 27–40. Fifth Asia-Pacific Conference on Wind Engineering.
Xu, Y.L., Li, Y.L., Shum, K.M., Kwok, K.C.F., Kwok, K.C.S., Hitchcock, P.A., 2006. Aerodynamic coefficients of inclined circular cylinders with artificial rivulet in smooth flow. Adv. Struct. Eng. 9 (2), 265–278.
Yamaguchi, H., 1990. Analytical study on growth mechanism of rain vibration of cables. J. Wind Eng. Ind. Aerodyn. 33 (1–2), 73–80.
Zaman, K., McKinzie, D., Rumsey, C., 1989. A natural low-frequency oscillation of the flow over an airfoil near stalling conditions. J. Fluid Mech. 202, 403–442.
Zhou, J., Adrian, R.J., Balachandar, S., Kendall, T.M., 1999. Mechanisms for generating coherent packets of hairpin vortices in channel flow. J. Fluid Mech. 387, 353–396.
Zuo, D., Jones, N., Main, J., 2008. Field observation of vortex-and rain-wind-induced stay-cable vibrations in a three-dimensional environment. J. Wind Eng. Ind. Aerodyn. 96 (6), 1124–1133.